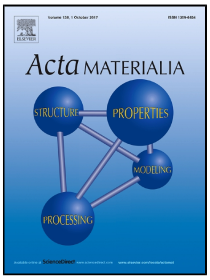

Understanding cementite dissolution in pearlitic steels subjected to rolling-sliding contact loading: A combined experimental and theoretical study

Hu Chen, Yanzhou Ji, Chi Zhang, Wenbo Liu, Hao Chen, Zhigang Yang, Long-Qing Chen, Lei Chen

PII:	S1359-6454(17)30753-X
DOI:	10.1016/j.actamat.2017.09.017
Reference:	AM 14047
To appear in:	*Acta Materialia*
Received Date:	04 May 2017
Revised Date:	15 August 2017
Accepted Date:	10 September 2017

Please cite this article as: Hu Chen, Yanzhou Ji, Chi Zhang, Wenbo Liu, Hao Chen, Zhigang Yang, Long-Qing Chen, Lei Chen, Understanding cementite dissolution in pearlitic steels subjected to rolling-sliding contact loading: A combined experimental and theoretical study, *Acta Materialia* (2017), doi: 10.1016/j.actamat.2017.09.017

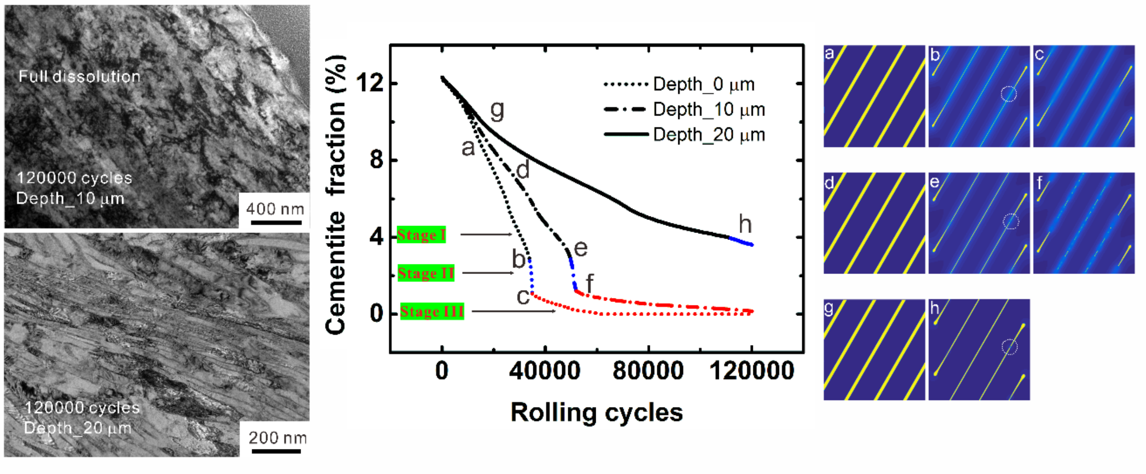
Full dissolution
120000 cycles
Depth_10 μm
400 nm
120000 cycles
Depth_20 μm
200 nm
Cementite fraction (%)
12
8
4
0
0
40000
80000
120000
Rolling cycles
Depth_0 μm
Depth_10 μm
Depth_20 μm
Stage I
Stage II
Stage III
a
b
c
d
e
f
g
h

Understanding cementite dissolution in pearlitic steels subjected to rolling-sliding contact loading: A combined experimental and theoretical study

Hu Chen [a, b], Yanzhou Ji [c], Chi Zhang [a, *], Wenbo Liu [d], Hao Chen [a], Zhigang Yang [a], Long-Qing Chen [c], Lei Chen [b, *]

a. Key Laboratory of Advanced Materials of Ministry of Education, School of Materials Science and Engineering, Tsinghua University, Beijing 100084, China

b. Department of Mechanical Engineering, Mississippi State University, MS 39762, USA

c. Department of Materials Science and Engineering, The Pennsylvania State University, University Park, PA 16802, USA

d. Department of Nuclear Science and Technology, Xi'an Jiaotong University, Xi'an 710049, China

Abstract

Cementite dissolution behavior of pearlitic steels subjected to rolling-sliding contact deformation is comprehensively investigated by combining experimental characterization and phase-field modeling. An elasto-plastic phase-field model, incorporating the elastic strain-induced free energy contribution from first-principles calculations and the plastic counterpart from a rolling-sliding contact finite element model assisted with a plastic strain accumulation model, is originally proposed to simulate the real-time evolution of cementite volume fraction, cementite morphology and carbon distribution for different rolling cycles and contact depths. Upon experimental validations, the proposed model predicts more accurate and realistic results than Sauvage's model. A three-stage behavior of cementite dissolution is also revealed, which well explains an experimentally observed significant cementite dissolution gradient along the depth direction. Besides, the effect of ferrite/cementite interface thickness and the initial lamellae thickness of cementite on cementite dissolution kinetics is studied. The proposed phase-field model can not only help understand the mechanism of cementite dissolution, but also give new sights into quantitative predictions of the mechanical properties and even the rolling contact fatigue life of pearlitic rail steels in service.

Keywords: rolling-sliding contact; phase-field model; cementite dissolution; microstructure evolution

[*]Corresponding author.
E-mail: chizhang@tsinghua.edu.cn (Chi Zhang) and chen@me.msstate.edu (Lei Chen)

1. Introduction

Rails are subjected to increasing mechanical wear and rolling contact fatigue (RCF) due to fast train speed [1] and massive axle loads [2] in modern railway systems. Therefore, there are surging interests to explore the underlying mechanism of material failures for improving the properties of existing rail steels and prolonging the service life of rails. Microstructure evolution in the surface layer of pearlitic rail steels has been well recognized to be closely related to the degradation of mechanical properties, the formation of microcracks, and eventually failure in rails [3, 4]. For example, White Etching Layer (WEL), a hard and brittle layer featured with so called "cementite dissolution" in the microstructure on rail surface is usually believed to be favorable locations of crack initiation, which is dramatically detrimental to the rail lifetime [5, 6]. However, the details of microstructure evolution in pearlitic rail steels during rolling-sliding contact deformation, including pearlite deformation, grain refinement of ferrite and especially dissolution of cementite, remains elusive due to the complicated interaction between the cyclic contact load, the frictional heat and complex microstructure characteristics. Therefore, there is currently a critical need to understand the fundamental mechanism of microstructure evolution of rail steels under rolling-sliding contact deformation.

A great number of experimental efforts have been made on microstructure characterization of rail surface during the past decades. Most of the experimental observations are focused on finding the evidences to support two categories of cementite dissolution mechanisms that are still in dispute, i.e., mechanical deformation induced dissolution vs. heat induced dissolution. Wild et al. [7] claimed that cementite dissolution was caused by frictional heat induced austenization and subsequent martensitic transformation, based on the experimentally observed retained austenite in rail surface. Takahashi et al. [8] estimated the temperature rise in rail surface from the concentration profile of Mn measured by three-dimensional atom probe (3DAP). They concluded that the temperature could reach 1300 °C at the topmost surface, which suggested that cementite dissolution occurred during rapid austenization caused by frictional heat. However, Fischer et al. [9] found that flash temperature could not exceed 500 °C even at the condition of maximum contact stress of 1500 MPa, 5% sliding ratio and velocity of 50 m/s. Considering that the austenitization temperature for eutectoid steel is 740 °C and does not decrease to less than 500 °C even at a much higher hydrostatic pressure [10], the austenitization by the temperature rise during normal rail–wheel contact conditions is not convincing [6]. Therefore, we tend to think that the austenite observed may be formed under some accidental extreme conditions, such as sudden brake [8], which can cause an enough local temperature rise for austenization. With increasing evidences in severe plastic deformation induced cementite dissolution by high pressure torsion [11] and cold drawing [12], Lojkowski et al. [13] proposed that the mechanism of cementite dissolution in rail surface was more likely driven by the severe plastic deformation. More specifically, they stated that the transformation can take place at a temperature of less than 230 °C after cyclic rolling-sliding contact deformation. By eliminating the effect of frictional heat, Chen et al. [14] recently confirmed that the cementite dissolution is caused by cyclic plastic deformation rather than frictional heat induced austenization under their experimental parameters. Although the mechanism of cementite dissolution under rolling-sliding condition is still a highly controversial issue, it is reasonable to postulate that mechanical deformation is one of the dominant factors under most experimental conditions.

Tremendous research works have been performed to understand how mechanical deformation drives cementite dissolution. As reviewed in Ref. [15], there are generally two potential underpinnings of cementite dissolution under severe loadings. Gridnev et al. [16, 17] proposed that the cementite dissolution may be induced by the difference between the binding energy of carbon interstitials and dislocations and the binding energy of carbon atoms and iron atoms in cementite under mechanical deformation. On the other hand, Languillaume et al. [18] thought that cementite dissolution is possibly contributed by the increase of free energy of cementite from thinning of cementite lamellae and formation of slip steps caused by plastic deformation. By extending Languillaume's model, Sauvage et al. [19] semi-quantitatively calculated cementite dissolution rate in cold-drawn pearlitic wires based on a diffusion-controlled dissolution process. Unfortunately, the predicted dissolution rates appeared to be underestimated in comparison with the experimental measurements. Further, the work was limited to cold-drawn pearlitic wires and cold-worked pearlitic steels in which the mechanical deformation is applied in the fashion of only one or a few cycles. Pearlitic rail steels, however, have to endure thousands of rolling-sliding contact deformation cycles during service. The cementite dissolution behaviors in pearlitic rail steels under cyclic loading may differ significantly from that in the simply cold-drawn pearlitic wires.

More recently, Nematollahi et al. [20] suggested that in addition to the contribution from the plastic deformation, an elastic strain-tuned free energy can be another potential contributor to cementite dissolution according to first-principles calculations. However, all of these existing studies are still at the early “hypothetical” stage where at most, only semi-quantitative calculations were conducted on the cementite dissolution of pearlitic steels. A reliable model integrating such two factors and how these two factors intrinsically contribute to the cementite dissolution is still not available.

In the present study, an elasto-plastic phase-field model, integrating an elastic strain and plastic strain induced free energy increase in cementite and ferrite, is originally proposed to understand the fundamental mechanism of mechanical deformation induced cementite dissolution. Upon the experimental validation, the proposed model has been demonstrated to achieve a quantitative estimation of cementite dissolution kinetics in cold-drawn pearlitic wires. The validated model is then applied to a pearlitic steel under cyclic rolling-sliding contact deformation. The simulated cementite volume fraction, cementite morphology and carbon distribution are then directly compared with the results after rolling-sliding contact experiments.

The present elasto-plastic phase-field model is applicable to the cementite dissolution in pearlitic steels under various manufacturing or serving conditions.

2. Experimental methods

A hypereutectoid pearlitic steel is used in the present study; the details of heat treatment and experimental setup are given in [14]. Torque and friction coefficients are recorded by torque transducer and are then used as input parameters for the rolling-sliding contact finite element model. Table 1 lists the rolling-sliding contact experimental parameters in the present study. The applied load is 1500 N, and the sliding ratio between the up and bottom discs is 0.5%. The only different parameter between sample A and sample B is the number of rolling cycles, which is 30000 cycles for sample A and 120000 cycles for sample B.

After rolling-sliding contact experiments, longitudinal sections of the discs are prepared for scanning electron microscopy (SEM) through mechanical grinding and polishing followed by etching in 4% solution of HNO_3 in ethanol. Transmission electron microscopy (TEM) samples at different depths below the contact surface are prepared by focused ion beam (FIB). TEM characterization is conducted on JEM-2100F with an operating voltage of 200 kV.

3. Model description

In this study, a multiscale computational framework, in which an elasto-plastic phase-field model is coupled with the finite-element method, is proposed to model the cyclic mechanical deformation-driven cementite dissolution. The distributions of stress and strain as functions of rolling cycles and contact depths, at the macro-scale, are first calculated by a rolling-sliding contact finite element model. The accumulated strain is then fed into the phase-field model to simulate the real-time evolution of cementite volume fraction, cementite morphology and carbon distribution at the meso-scale.

3.1. Finite-element model

To improve the computation efficiency, a 2-D plane strain finite element model [21] is employed to simulate the stress distribution in the rolling-sliding experiment instead of a 3-D model. The rolling disc used in the experiment is 60 mm in diameter and 10 mm in thickness. A circular segment with height of 6 mm of the disc is used in the simulation. The penalty function methods are used to solve the contact and friction problem. Contact load and friction torque applied are 1500 N and 18 Nm respectively, from rolling-sliding experiments. The Young's modulus and the Poisson's ratio of the rail are set as 210 GPa and 0.3. The yield strength and tensile strength are 490 MPa and 900 MPa, respectively.

3.2. Plastic strain accumulation model

The model proposed by Kapoor and Franklin [22] is used to calculate the plastic strain accumulation as a function of rolling cycles and contact depths, with the input of shear stress distribution from finite element calculations and material hardening behavior from literature [23]. The shear strain increment after a new rolling cycle at the depth of z is given by [23]:

$$\Delta\varepsilon_p^{[z]} = C\left(\frac{\tau_{zx(\max)}^{[z]}}{k_{eff}^{[z]}} - 1\right) \tag{1}$$

where $\tau_{zx(\max)}^{[z]}$ is the maximum shear stress at the depth of z, $k_{eff}^{[z]}$ is the effective shear strength of material at the depth of z, and C has a constant value of 0.00237 [24].

The total accumulated shear strain is then calculated by:

$$\varepsilon_p^{[z]} = \sum_N \Delta\varepsilon_p^{[z]} \tag{2}$$

where N is the number of rolling cycles. When the total accumulated strain exceeds a critical value, for example 11 according to Tyfour's experimental measurement [25], no further deformation is considered. Because the material detachment is provisionally neglected in the present study, the strain distribution was considered unchanged after the corresponding cycles.

Work-hardening is considered by a modified Voce equation [23]:

$$\frac{k_{eff}}{k_0} = \max\left\{1, \beta\sqrt{1-\exp(-\alpha\varepsilon_p)}\right\} \tag{3}$$

where the constants $\alpha = 1.0$ is a measure of how quickly the material hardens, and $\beta =$ 1.45 a measure of how much it hardens. $k_0 = \sigma_y / \sqrt{3}$ is the initial shear yield stress from von Mises's strain-energy criterion.

3.3. Phase-field model

Accurate prediction of cementite dissolution kinetics relies on meso-scale computational models that can quantitatively evaluate the thermodynamic driving force and kinetic mechanisms of the dissolution process. For this purpose, the phase-field approach is a desirable candidate which has been applied to simulate various meso-scale phenomena including pearlite transformation [26-28].

As the cementite dissolution under deformation is a complicated problem involving different energy contributions, especially the plastic energy, while the phase-field models with elasto-plastic constitutive relations and governing equations are still at the early development stages, related phase-field investigations on cementite dissolution in pearlite steels under mechanical deformation are still rare. Therefore, we propose a novel phase-field model integrating both elastic and plastic deformation to simulate the cementite dissolution, with an application to the rail steels during the cyclic rolling-sliding contact.

3.3.1. Formulations

In this model, a continuous phase-field variable, ϕ, is introduced to distinguish the ferrite ($\phi = 0$) and cementite ($\phi = 1$) during cementite dissolution. The carbon distribution in the phases is described by the concentration field, c. Specifically, c^{α} and $c^{\mathrm{Fe_3C}}$ represent the carbon composition (in atomic ratio) of the two phases, respectively. The Kim-Kim-Suzuki (KKS) model [29] is employed due to its accuracy in modeling stoichiometric compounds (cementite in the present study) with sharp curvature of free energy functions. The total free energy F_{total} of the system is given by:

$$F_{total} = \int_V \left[\frac{1}{\Omega_0} f_{local}(c,\phi,\varepsilon) + \frac{\kappa}{2} |\nabla \phi|^2 \right] dV \tag{4}$$

where Ω_0 is the molar volume of the system [30], and $f_{local}(c,\phi,\varepsilon)$ is the local free energy, which is related to carbon concentration c, phase-field variable ϕ and strain ε. The second gradient term partially accounts for the interfacial inhomogeneity between two phases where κ is a gradient coefficient.

In KKS model, the interface is assumed to be a mixture of two phases. Hence

$$f_{local}(c,\phi,\varepsilon)=[1-p(\phi)]f^{\alpha}(c^{\alpha},\varepsilon)+p(\phi)f^{\mathrm{Fe_3C}}(c^{\mathrm{Fe_3C}},\varepsilon)+g(\phi) \tag{5}$$

where f^{α} and $f^{\mathrm{Fe_3C}}$ are the free energy of ferrite and cementite, respectively, $p(\phi)=\phi^3(6\phi^2-15\phi+10)$ is an interpolation function, $g(\phi)=\phi^2(1-\phi)^2 w$ is a double-well potential and w is the barrier height.

The key novelty of the current phase-field model is to involve both the elastic strain and plastic strain contributions, which will be referred to as elastic part and plastic part in the following description, in f^{α} and $f^{\mathrm{Fe_3C}}$:

$$f^{\alpha}=f^{\alpha}_{chem}(c^{\alpha})+f^{\alpha}_{el}(\varepsilon_e)+f^{\alpha}_{pl}(\varepsilon_p) \tag{6}$$

$$f^{\mathrm{Fe_3C}}=f^{\mathrm{Fe_3C}}_{chem}(c^{\mathrm{Fe_3C}})+f^{\mathrm{Fe_3C}}_{el}(\varepsilon_e)+f^{\mathrm{Fe_3C}}_{pl}(\varepsilon_p) \tag{7}$$

where f^{α}_{chem} and $f^{\mathrm{Fe_3C}}_{chem}$ are the chemical free energy of ferrite and cementite, respectively. The chemical free energy of ferrite follows the work of Loginova [31, 32], which is based on regular solution model. The chemical free energy of cementite is described by a parabolic function with equal first derivative, i.e., a common tangent line of two chemical free energy functions as illustrated in Fig. 1(b), and second derivative to those of ferrite at each equilibrium composition.

The elastic part, $f^{\alpha}_{el}(\varepsilon_e)$ and $f^{\mathrm{Fe_3C}}_{el}(\varepsilon_e)$, accounting for the lattice distortion of cementite and ferrite crystals, are obtained by fitting the total energy of bcc Fe and cementite as a function of elastic strain of Ref. [20] into a parabolic function:

$$f_{el}^{\alpha}(\varepsilon_e) = A^{\alpha}\varepsilon_e^2 + B^{\alpha}\varepsilon_e + C^{\alpha} \tag{8}$$

$$f_{el}^{\mathrm{Fe_3C}}(\varepsilon_e) = A^{\mathrm{Fe_3C}}\varepsilon_e^2 + B^{\mathrm{Fe_3C}}\varepsilon_e + C^{\mathrm{Fe_3C}} \tag{9}$$

where *A*, *B* and *C* are fitting parameters listed in Table 2, ε_e is the elastic strain and 1.0% is used in present simulation for both phases [33].

The plastic part is attributed to the increase of the sub-interfaces resulting from the plastic deformation. Specifically, upon heavy plastic deformation, dislocations are accumulated at interfaces (Fig. 1(a-I)) as a consequence of strain incompatibilities between ferrite and cementite lamellae. The local stress rise at interface can facilitate the formation of slip steps within the cementite lamellae [18], which induces the free energy increase due to the appearance of sub-interfaces. In this study, for simplicity, rather than considering the detailed microscopic deformation mechanisms, we approximately consider the plastic strain energy contributions as part of local free energy. As the thickness of cementite lamellae is considerably smaller than that of ferrite, the surface to volume ratio increase in cementite should be significantly larger than that of ferrite lamellae. According to Sauvage [19], the increase of free energy per unit volume in ferrite, $f_{pl}^{\alpha}(\varepsilon_p)$, due to contribution of plasticity-induced sub-interfaces is only one ninth of that of cementite, $f_{pl}^{\mathrm{Fe_3C}}(\varepsilon_p)$, (Fig. 1(a-II)) and is thus considered negligible in the simulation [19].

The plastic part $f_{pl}^{\mathrm{Fe_3C}}(\varepsilon_p)$ in cementite phase is then estimated using a linear approximation [19]:

$$f_{pl}^{\mathrm{Fe_3C}}(\varepsilon_p) = \gamma V_m \frac{1+\ln(1+\varepsilon_p)}{t} \qquad (10)$$

where γ is the ferrite/cementite interfacial energy without plastic deformation, V_m is the molar volume of cementite and t is the lamellar thickness of cementite, ε_p is the plastic strain accumulated during the rolling-sliding contact deformation calculated from the plastic strain accumulation model (Eq. (2)), which is dependent on contact depth and the number of rolling cycles.

The molar free energy of ferrite and cementite versus composition is plotted in Fig. 1(b). Prior to the mechanical deformation, the equilibrium state of ferrite is given by point A with the equilibrium carbon composition of c^{α}. As the mechanical deformation accumulates, the molar free energy the cementite increases compared to that of the ferrite, expressed as $\Delta F = f_{el}^{\mathrm{Fe_3C}}(\varepsilon_e) + f_{pl}^{\mathrm{Fe_3C}}(\varepsilon_p) - f_{el}^{\alpha}(\varepsilon_e) - f_{pl}^{\alpha}(\varepsilon_p)$, thus resulting in a thermodynamic destabilization of cementite according the minimum energy principles. Consequently, the equilibrium carbon concentration (at.%) will increase from c^{α} to c_{ε}^{α} from the common tangent rule after mechanical deformation. If the local equilibrium at ferrite/cementite interface is assumed, then cementite is locally destabilized. Hence a carbon concentration gradient will appear between the lamellae and will induce the dissolution of cementite from the interfaces. Further, carbon diffusion in ferrite will lead to an overall concentration increase in ferrite as shown in the inserted picture in Fig. 1(b).

The spatial and temporal evolutions of composition and order parameters are governed by the Cahn–Hilliard equation [34] and Allen–Cahn equation [35], respectively:

$$\frac{\partial c}{\partial t}=\nabla\cdot\left[\frac{D(T)}{(f_{local})_{cc}}\nabla\frac{\partial f_{local}}{\partial c}\right]=\nabla\cdot\left[M(T)\nabla\frac{\partial f_{local}}{\partial c}\right] \tag{11}$$

$$\frac{\partial\phi}{\partial t}=-L\frac{\delta F}{\delta\phi}=\frac{L}{\Omega_0}\left[-\frac{\partial f_{local}}{\partial\phi}+\Omega_0\kappa\nabla^2\phi\right] \tag{12}$$

where $D(T)$ and $M(T)$ are chemical diffusivity and mobility, respectively, $(f_{local})_{cc}$ is the second derivative of f_{local}, and L is the interface mobility coefficient.

Based on KKS model, the equal chemical potential constraint condition becomes,

$$c=[1-p(\phi)]c^{\alpha}+p(\phi)c^{\mathrm{Fe_3C}} \tag{13}$$

$$\frac{\partial f^{\alpha}(c^{\alpha},\varepsilon)}{\partial c^{\alpha}}=\frac{\partial f^{\mathrm{Fe_3C}}(c^{\mathrm{Fe_3C}},\varepsilon)}{\partial c^{\mathrm{Fe_3C}}} \tag{14}$$

3.3.2. Model parameters

We assume that the diffusion coefficient $D(T)$ in Eq. (11) only depends on temperature T,

$$D(T)=D_0\exp[-\frac{Q}{RT}] \tag{15}$$

where D_0 is the prefactor of the diffusion constant, Q is the activation energy of carbon diffusion, R is the universal gas constant.

Three unknown phase-field parameters, κ, w and L, are involved in the kinetic equation, i.e., Eq. (12). The gradient coefficient κ and barrier height w are related to interfacial energies γ and interface thickness 2λ [36].

$$\gamma=\frac{\sqrt{\kappa\cdot(w/\Omega_0)}}{3\sqrt{2}} \tag{16}$$

$$2\lambda = a\sqrt{2}\sqrt{\frac{\kappa}{w/\Omega_0}} \tag{17}$$

where a is a constant which depends on the definition of the interface. The interface thickness of ferrite/cementite is defined as a measure of the changes of the phase-field variable from 0.1 to 0.9. Experimental measured carbon concentration profile across the ferrite/cementite interface [37] in deformed pearlite was used to estimate the interface thickness. A sharp concentration gradient with a thickness of about 2.5 nm was observed across the ferrite/cementite interface [37]. In addition, along the interface at the cementite side there is a 10 nm-thick layer with a carbon content in a range of 20–25 at.% which could be attributed to the off-stoichiometry cementite. According to the definition of interface thickness in the present study, if $\phi < 0.9$ at the cementite side is considered as interface, i.e. carbon concentration less than 90% of the stoichiometry concentration (25 at.%) of cementite, another 3 nm will belong to the interface. As a consequence, the use of interface thickness between 2nm to 6nm is reasonable if the effect from off-stoichiometry of cementite is partial taken into consideration.

Phase-field mobility is practically calculated according to the following equation [38]:

$$L = k \cdot M_p \cdot \frac{\gamma}{\kappa} \tag{18}$$

where k is a fitting parameter and M_p is the physical ferrite/cementite interface mobility from Ref. [26].

In summary, the simulation of cementite dissolution reduces to the solution of the kinetic Eq. (11) and Eq. (12) under the constraint conditions Eq. (13) and Eq. (14). Both kinetic equations are solved in Fourier space [39, 40] using the FFT algorithm in reduced units, with nondimensionalizing factors $E = 1.18 \times 10^{11}$ J/m^3 and $l = 10^{-9}$ m. Hence the dimensionless simulation time step t^* is related to the real time by a nondimensionalizing factor D/l^2. The real contact time in one cycle, t_c, is calculated from contact zone, which is measured to be about 0.3 mm from stress distribution of the finite element model, and rotation speed (500 r/min) of the rolling-sliding contact experiment. Therefore, the rolling cycles in experiments are connected to the simulation cycles in the present model.

Based on these model parameters, a 2-D phase-field model with a size of 600 × 600 grid, representing a physical domain of 600 nm × 600 nm, is employed. Unless otherwise specified, the interface thickness (2λ) is 4 nm in the present simulation. The modelling temperature is 600K for all rolling-sliding simulations to capture the effect of friction induced temperature rise at the contact surface. The model parameters used in present simulation are summarized in Table 2.

4. Model validation

The proposed phase-field model is first validated by comparing the cementite dissolution rate with Sauvage's prediction and the existing experimental results in cold-drawn wires, and the results, i.e., the amount of dissolved cementite after cold drawing as a function of temperature are shown in Fig. 2. The parameters used in the validated case all follow those of Sauvage's work [19], in which the wire temperature is 200 °C, the true logarithmic strain is 3.5 and the interlamellar spacing of pearlite is 90 nm. When the temperature decreases to 100 °C, the dissolution amount from phase-field simulations, either with or without the elastic energy, agrees well with the experimentally measured amount, in contrast to Sauvage's model [19] which presents a clear (70%) underestimation of the dissolved amount. As the ferrite/cementite interface thickness decreases to 1.3 nm, close to the grid size, the prediction of present phase-field model converges to Sauvage's model. Hence the discrepancy between the above two models is primarily attributed to the difference in the description of the ferrite/cementite interface. In Sauvage's model, a sharp interface and a constant carbon concentration (25 at.%) in cementite were considered; whereas a diffuse interface with certain thickness based on experimental measurement [37] is proposed in the present phase-field model. The simulated carbon concentration gradient at the cementite side of the ferrite/cementite interface is more consistent with the experimental results measured by 3DAP [41], as shown in the inserted picture in Fig. 2, which justifies the rationality of the concept of diffuse interface. Another salient observation is the model with the elastic energy clearly outperforms the counterpart without the elastic contribution, when compared with the experimental measurements at the same strain level [12]. Consequently, we rationalize the necessity of the contribution by the elastic strain in the free energy, in addition to the plastic contribution. The phase-field model, integrating both elastic and plastic energy, is subsequently applied to the pearlitic steels subjected to the cyclic rolling-sliding contact deformation.

5. Results and Discussions

5.1. FEM results: stress and strain distributions

The distribution of shear stress of discs under rolling-sliding contact loading is shown in Fig. 3(a). The concentrated stress pattern in the surface region of about 3 mm in thickness indicates the rationality of using a circular segment with a height of 6 mm in the rolling-sliding contact finite element model. An enlarged picture of the contact zone in Fig. 3(b) indicates the maximum shear stress of 543 MPa at the top surface and the plastic region, i.e., where the shear stress is larger than the shear strength of the material, within the 200 μm region. Fig. 3(c) plots the maximum shear stress as a function of the depth, which decreases linearly to 410 MPa with the depth increasing to 50 μm, stays constant in the next 25 μm, and then gradually decreases to 300 MPa at the depth of 200 μm.

The accumulated plastic strain as a function of rolling cycles is shown in Fig. 3(d). With the increase of rolling cycles, the strains at all depths display a continuous accumulation during the first 14000 cycles. Moreover, the plastic strain accumulation rate, as shown by the slope of the curves in Fig. 3(d), is much faster at surface layers. After 14000 cycles, the accumulated plastic strains reach the critical strain at the contact surface, and the plastic strain accumulation at all depths will stop. The maximum plastic strains at depths of 0 μm, 10 μm, 20 μm, 30 μm, 40 μm, 60 μm and

100 μm are 11.00, 9.18, 7.13, 4.98, 3.21, 2.65 and 2.00, respectively.

5.2. Phase-field results: cementite dissolution

The elasto-plastic phase-field model, fed by the accumulated plastic strain above, is subsequently applied to the pearlitic steels subjected to cyclic rolling-sliding contact deformation. The initial interlamellar spacing of pearlite is set as 150 nm and the volume fraction of cementite is 12%, i.e., the initial lamellar thickness of cementite is 18 nm, as determined from the experiments. For the purpose of experimental validation, rolling-sliding contact experiments are conducted on the pearlitic steels, and cementite morphology and cementite dissolution amount are then characterized by SEM and TEM.

5.2.1. Cementite morphology evolution

The simulated evolution of cementite morphology during cyclic rolling at different depths is shown in Fig. 4. The cementite dissolution rate decreases with the increase of the depth, as reflected from the thinning rate of the cementite lamellae, the number of rolling cycles for the initiation of discontinuity in the cementite lamellae, and the number of rolling cycles for the full cementite dissolution.

The fastest dissolution rate is achieved at the contact surface, i.e., at the depth of 0 μm. The thickness of cementite lamellae decreases to 2.7 nm and starts to show discontinuity or breakage at 34700 rolling cycles, until full dissolution after 60000 cycles. In comparison, although cementite is almost fully dissolved at 10 μm below the contact surface after 90000 cycles, the breakage of cementite appears at 50000 cycles with an average cementite thickness of 4.0 nm.

At the depth of 20 μm, there is still 3.6 vol.% cementite left after 120000 cycles, and the breakage of cementite shows up at 110750 cycles with a much larger cementite thickness of 5.8 nm. At the depth of 30 μm, however, only decrease in the thickness of cementite lamellae is observed in the morphology profile after 120000 cycles, without any breakage.

The dissolution rate of cementite, as well as the critical thickness for the breakage of cementite lamellae, is related to the free energy increase due to accumulated plastic strain. With the increase of depth, the decreased accumulated plastic strain results in decreased ΔF, reducing the dissolution driving force and therefore retarding the cementite dissolution rate.

Fig. 5 shows the TEM images of different depths below the contact surface of the sample after 120000 rolling cycles. At the center of the sample (Fig. 5(a)), i.e. at depth of about 5 mm, the pearlite structure appears unperturbed and the interlamellar spacing is about 150 nm, the same as that of the sample after heat treatment. For the depth of 10 μm as in Fig. 5(b), however, original ferrite and cementite lamellae structure can hardly be observed. Only diffraction rings from ferrite are detected and no diffraction spot from cementite is observed in the selected area electron diffraction (SAED) pattern, which suggests a full decomposition of cementite at the depth of 10 μm. This observation is well consistent with the simulated results shown in Fig. 5(c), in which a full dissolution of cementite is also witnessed at the depth of 10 μm after

120000 rolling cycles.

Fig. 5(d) shows the TEM image at the depth of 20 μm. Large proportion of pearlite with an interlamellar spacing of around 40 nm and relatively high dislocation densities are observed. Such an observed feature is in accordance with that of high pressure torsion [42] and drawn pearlite [43].

To further achieve a direct comparison between the experimental and simulated morphology of cementite lamellae for the depth of 20 μm, high resolution transmission electron microscopy (HRTEM) study is conducted on the microstructure in the rectangle in Fig. 5(d). From the HRTEM and the fast Fourier transform (FFT) pattern from the region of the white rectangle in Fig. 5(e), the thin lamellae are identified as undissolved cementite phase. It can be observed that the thickness of cementite lamellae ranges from 5~10 nm. The cementite lamellae are not continuous; instead, micro-breakages show up as pointed out by the arrows, indicating nonuniform dissolution of cementite at this stage. Under the same rolling cycle and depth, the simulated lamellar thickness of cementite is 5.3 nm with breakages in cementite lamellae, as shown in Fig. 5(f), which is consistent with the simulated microstructure.

Such an agreement in microstructure morphology confirms the capability of the proposed phase-field model for simulating the morphology evolution of cementite lamellae at arbitrary rolling cycles and contact depths. As the mechanical properties of pearlitic rail steel are mainly determined by the morphology of cementite, the service performances and even the RCF life of rail steels may be predicted with the accurate simulation of microstructure evolution at hand.

5.2.2. Cementite thickness and deformed layer

The simulated thickness variations of cementite lamellae as a function of rolling cycles at various contact depths are displayed in Fig. 6(a). At the depth of 0 μm, the thickness of cementite lamellae decreases dramatically to 6.1 nm in the first 30000 cycles before a huge drop to 1.6 nm during 30000 to 35000 cycles. At the depth of 10 μm, the cementite thinning rate is lower with the huge drop coming up at 45000 cycles. Complete dissolution is observed in these two depths; in contrast, at the depth of 20 μm, the cementite thickness gradually decreases to 5.3 nm at 120000 cycles. For depths of more than 40 μm, the thickness of cementite lamellae shows slight decreases from 18 nm to 14.8 nm at the depth 40 μm, to 15.3 at the depth 60 μm and to 15.8 nm at the depth 100 μm in the first 50000 cycles and then stays almost constant.

The simulated cementite lamellae thicknesses as a function of depth after 30000 cycles and 120000 cycles are shown in Fig. 6(b). If the position where the thickness of cementite lamellae is 70% of its original value, i.e. 12.6 nm in present simulation, is chosen as the boundary between the deformed layer and the undeformed matrix, the calculated deformed layer depth is 21 μm after 30000 cycles and increases to 32 μm after 120000 cycles as shown by the color bars in Fig. 6(b), which indicates a deformation accumulation process with rolling cycles.

The SEM micrographs of cross sections of the rolling-sliding samples after

30000 cycles and 120000 cycles are shown in Fig. 6(c) and (d), respectively. A heavily deformed layer, in which the pearlite structure is aligned along the rolling surface under the shear stress, is identified in both samples. The thickness of the deformed layer increases with rolling cycles, from 25 μm at 30000 cycles to about 45 μm at 120000 cycles. Although the absolute value of the experimental measured deformed thickness is slightly higher than the simulated results in Fig. 6(b), the similar changing trend suggests the capability of the current phase-field model to capture the overall deformation process.

5.2.3. Cementite composition change

Fig. 7(a), (b) and (c) show the simulated carbon concentration profile in cementite and ferrite lamellae as a function of rolling cycles at the depth of 0 μm, 10 μm and 20 μm respectively. In the contact layer (Fig. 7(a)), with the increase of the rolling cycle, the ferrite/cementite interface moves towards cementite and the carbon concentration in ferrite increases. After 30000 cycles, only the inner 1–2 nm of the cementite lamellae with an average thickness of 6.1 nm (Fig. 6(a)) keeps the concentration of 25 at.%. With increasing rolling cycles, the maximum carbon content in cementite is decaying, 18.9 at.% at 34700 cycles and to 8.4 at.% at 35000 cycles, until full cementite dissolution. At the depth of 10 μm (Fig. 7(b)), the overall evolution trend is similar to that of the contact layer but at a relative low evolution speed. In Fig. 7(c), however, no carbon concentration decrease is observed at the center of cementite lamellae even after 120000 rolling cycles.

The calculated carbon concentration profile in the heavily deformed layer, which is apparently lower than the stoichiometry concentration of carbon in cementite, is similar to the 3DAP measurement in literature [6, 8, 41, 44]. For example, a comparison between the simulated carbon concentration after 51150 cycles at the depth of 10 μm and the measured carbon concentration of deformed pearlite on rail surface by Zhang et.al [6] is shown in Fig. 7(d). Both simulated and experimentally measured carbon concentration profiles show a maximum carbon concentration in the range of 9–10 at.% at the position of prior cementite lamellae. The carbon concentration then gradually decreases to about 2.5–3.0 at.% in ferrite, which is much higher than the equilibrium carbon concentration of ferrite in undeformed state.

As carbon concentration in cementite lamellae can deviate from its stoichiometry concentration during the dissolution process, the diffuse interface assumption of the ferrite/cementite interface is more realistic than the sharp interface assumption, which accounts for the accuracy of the present phase-field model when compared with Sauvage's model.

5.3. Cementite dissolution kinetics

As complex microstructure characteristics are often observed on rail surface, the mechanism of microstructure evolution is still in dispute. It is inferred that those different microstructures may result from different stages of the microstructure evolution process, so the study of dissolution kinetics of cementite may shed lights on some highly controversial phenomena observed on rail surface.

5.3.1. Three-stage dissolution kinetics

In the present simulation, as revealed in Fig. 8(1), cementite lamellae show a three stages dissolution behavior. In stage I, cementite displays a linear dissolution rate due to the increase of free energy as indicated by line a–b, d–e and g–h. At the transition point between stage I and II, discontinuity or breakage starts to appear in cementite lamellae as shown by the dot circles in the simulated carbon concentration profiles b, e and h. The increase of interface area when the cementite breaks can significantly enhance the dissolution kinetics in stage II. In addition, the curvature at the surface of the breakage part is much larger than the plain interface between the prior ferrite and cementite lamellae, which can lead to a fast shortening of cementite lamellae due to the Gibbs-Thomson effect. Consequently, a steep dissolution behavior is observed in stage II as shown by line b–c and e–f. At the end of stage II, the interfaces between ferrite and cementite lamellae become vague and only some small particles located at prior cementite lamellae are left in c and f. In stage III, spheroidization of cementite and diffusion of carbon atoms are achieved.

It should be noted that the cementite dissolution behavior is strongly dependent on the depth. For example, since the free energy increase due to the accumulated plastic strain is decreasing with increasing depth, the dissolution driving force and therefore dissolution kinetics are decreasing, leading to the incompleteness of the three kinetic stages at high depth. More importantly, due to the fast dissolution kinetics in stage II, the “transition zone” for different kinetic stages in the sample after certain rolling cycles is quite sharp. As illustrated in Fig. 8(2), after 120000 cycles, the volume fractions of cementite at depths of less than 17.5 μm are all well below 1.0%, showing an almost full dissolution behavior. However, at the depth of 20 μm, 3.6% cementite is present with an average lamellae thickness of 5.3 nm, indicating a sharp transition zone of less than 2.5 μm. It is worth noting that sharp boundaries between the WEL with complete cementite dissolution and the layer below are frequently observed experimentally under rail surfaces after service [6, 8, 13, 45] and are often used to support the heat induced cementite dissolution and WEL formation mechanism. In our simulation assuming the mechanical deformation-driven cementite dissolution mechanism, however, if the full dissolution regions are considered as the WEL, the sharp boundaries can also be realized due to the transition of the cementite dissolution kinetics.

5.3.2. Effect of elastic strain energy

As discussed in Section 4, the elastic strain-induced free energy contribution is a non-unimportant factor for cementite dissolution under cold drawing. In this section, we further study the effect of elastic contribution on cementite dissolution in rolling-sliding contact deformation, by comparing the cementite dissolution rate between two systems with and without elastic strain-induced energy. As shown in Fig. 9, the elastic strain-induced free energy strongly shifts the dissolution curve for depth of 0 μm and 10 μm. At the depth of 20 μm, the volume fraction of cementite for the system without elastic energy after 120000 rolling cycles is 6.2%, almost 2 times of that in the system with elastic energy. Hence the elastic strain-induced energy can accelerate cementite dissolution in rolling-sliding contact deformation more obviously than that in cold drawing (Fig. 2).

5.3.3. Effect of interface thickness

Understanding the effect of ferrite/cementite interface thickness on the dissolution kinetics can provide useful guidance for controlling the dissolution behavior of cementite by modifying the properties of ferrite/cementite interface. The volume fractions of cementite as functions of rolling cycles and contact depths of pearlite with different interface thicknesses are then calculated as shown in Fig. 10. At the depth of 0 μm and 10 μm, all three stages appear for all interface thicknesses during the 120000 cycles and the final volume fractions of cementite of different interface thicknesses for the same depth converge to a constant value, which is the thermodynamically equilibrium state determined by the common tangent line of strain-affected free energy in Fig. 1(b). For example, the equilibrium cementite volume fraction for the depth of 20 μm is 1.2%. At 120000 cycles, the simulated cementite volume fractions for interface thickness of 6 nm and 5 nm are 1.23% and 1.39%, respectively, quite close to the equilibrium fraction 1.2%. After another 60000 cycles, the volume fraction for interface thickness of 4 nm also decreases to 1.38%. Although the volume fraction predictions for interface thickness of 2 nm and 3 nm are still relatively high, it is safe to infer that the final equilibrium state will not be influenced by the interface thickness.

For different interface thicknesses, although the behaviors of stage I and stage III are similar, the transition between stage I and stage II is different. The larger the interface thickness, the earlier the appearance of stage II. Remember that the interface mobility is chosen according to Steinbach [26] to ensure a diffusion-controlled process, which means that the ferrite/cementite interface evolves ahead of carbon concentration and is dragged by carbon concentration. Only when carbon concentration catches up can the interface move forward. When the thickness of cementite lamellae decreases to the level of interface thickness, the drag force the carbon concentration imposes on the interface is no longer in effect. Consequently, interface can move forward freely instead of being dragged by carbon concentration at this state. The dissolution kinetics would start to enter into stage II. Hence the larger the interface thickness, the earlier the appearance of stage II for all depths shown in Fig. 10.

In conclusion, the cementite dissolution kinetics and the morphology evolution of cementite lamellae can be modified by ferrite/cementite interface thickness and interface properties, which is meaningful in controlling the cementite dissolution kinetics. Based on the comparison of the dissolution kinetics, cementite morphology and carbon concentration distribution between simulation and experiment, 4 nm is a reasonable interface thickness value in the present simulation.

5.3.4. Effect of initial cementite lamellar thickness

Apart from interface thickness, the effect of initial lamellar thickness of cementite or lamellar spacing of pearlite, is also investigated. Simulated volume fractions of cementite with three different initial lamellar thicknesses of cementite as a function of rolling cycles at the depth of 20 μm are shown in Fig. 11. The dissolution rate is found to increase with the decrease of initial thickness of cementite lamellae. As the lamellar thickness decreases from 22 nm to 18 nm and 14 nm, the average dissolution rate increases to 1.4 times and 2.75 times of its original value during the first 30000 rolling cycles. Although such a cementite dissolution behavior related to initial lamellae thickness is not reported in rail surface, a microstructural threshold of cementite dissolution was studied in cold drawn pearlitic steel wires [12]. It was reported that the strain for coarse pearlite to start to dissolve was larger than that for fine pearlite and the dissolution in coarse pearlite did not proceed any more at certain level of cementite fraction, which is similar to the case of cementite with initial thickness of 22 nm in the present simulation. This can be attributed to the decreased dissolution driving force with the increase of lamellar thickness, as shown in Eq. (10).

6. Conclusions

An elasto-plastic phase-field model is, for the first time, proposed to simulate mechanical deformation-driven cementite dissolution behavior of pearlitic steels under cyclic rolling-sliding contact deformation, which can deepen the understanding of the mechanism of cementite dissolution. The simulated results are then compared with the experimental characterization of pearlitic steels subjected to rolling-sliding contact loading in cementite dissolution amount, cementite morphology and carbon distribution. The following conclusions can be drawn:

- The proposed elasto-plastic phase-field model can well predict the evolution of cementite volume fraction, cementite morphology and carbon distribution of pearlitic steel subjected to rolling-sliding contact loading.
- A three-stage dissolution kinetics of cementite lamellae is determined from the phase-field simulations. Because of the kinetics transition, a great microstructure gradient is predicted along the contact depth, which well explains an experimentally observed sharp microstructure transition along the depth direction.
- Interface thickness is found to be a dominant factor in determining the dissolution transition between and stage I and stage II; and the initial thickness of cementite will shift the dissolution curve.

The proposed elasto-plastic phase-field model can be potentially extended to simulate cementite dissolution of pearlitic steel under various serving conditions. Future work is suggested to study the relationship between cementite dissolution behavior and the evolution of mechanical properties and thus RCF of rail steels in service.

Acknowledgements

Financial support from the National Basic Research Programs of China (No.2015CB654802), the National Magnetic Confinement Fusion Energy Research Project of China (2015GB118001), and National Natural Science Foundation of China (Grant No. 51471094) is acknowledged. The authors also gratefully acknowledge the financial support provided by Tsinghua University Scholarship Council for Graduate Overseas Studies. Lei Chen is grateful for the financial support by the Start-up funding from Mississippi State University.

References

[1] H.H. Ding, Z.K. Fu, W.J. Wang, J. Guo, Q.Y. Liu, M.H. Zhu, Investigation on the effect of rotational speed on rolling wear and damage behaviors of wheel/rail materials, Wear 330 (2015) 563-570.

[2] Y. Zhou, S. Wang, T. Wang, Y. Xu, Z. Li, Field and laboratory investigation of the relationship between rail head check and wear in a heavy-haul railway, Wear 315 (2014) 68-77.

[3] J.E. Garnham, C.L. Davis, The role of deformed rail microstructure on rolling contact fatigue initiation, Wear 265 (2008) 1363-1372.

[4] R. Carroll, J. Beynon, Rolling contact fatigue of white etching layer: Part 1: Crack morphology, Wear 262 (2007) 1253-1266.

[5] J. Seo, S. Kwon, H. Jun, D. Lee, Numerical stress analysis and rolling contact fatigue of White Etching Layer on rail steel, Int. J. Fatigue 33 (2011) 203-211.

[6] H.W. Zhang, S. Ohsaki, S. Mitao, M. Ohnuma, K. Hono, Microstructural investigation of white etching layer on pearlite steel rail, Mater. Sci. Eng. A 421 (2006) 191-199.

[7] E. Wild, L. Wang, B. Hasse, T. Wroblewski, G. Goerigk, A. Pyzalla, Microstructure alterations at the surface of a heavily corrugated rail with strong ripple formation, Wear 254 (2003) 876-883.

[8] J. Takahashi, K. Kawakami, M. Ueda, Atom probe tomography analysis of the white etching layer in a rail track surface, Acta Mater. 58 (2010) 3602-3612.

[9] F. Fischer, W. Daves, E. Werner, On the temperature in the wheel–rail rolling contact, Fatigue & Fracture of Engineering Materials & Structures 26(10) (2003) 999-1006.

[10] L. Blackburn, L. Kaufman, M. Cohen, Phase transformations in iron-ruthenium alloys under high pressure, Acta metallurgica 13(5) (1965) 533-541.

[11] F. Wetscher, A. Vorhauer, R. Stock, R. Pippan, Structural refinement of low alloyed steels during severe plastic deformation, Mater. Sci. Eng. A 387 (2004) 809-816.

[12] W.J. Nam, C.M. Bae, S.J. Oh, S.-J. Kwon, Effect of interlamellar spacing on cementite dissolution during wire drawing of pearlitic steel wires, Scripta. Mater. 42(5) (2000) 457-463.

[13] W. Lojkowski, M. Djahanbakhsh, G. Bürkle, S. Gierlotka, W. Zielinski, H.-J. Fecht, Nanostructure formation on the surface of railway tracks, Mater. Sci. Eng. A 303 (2001) 197-208.

[14] H. Chen, C. Zhang, W.B. Liu, Q.H. Li, H. Chen, Z.G. Yang, Y.Q. Weng, Microstructure evolution of a hypereutectoid pearlite steel under rolling-sliding contact loading, Mater. Sci. Eng. A 655 (2016) 50-59.

[15] V. Gavriljuk, Decomposition of cementite in pearlitic steel due to plastic deformation, Mater. Sci. Eng. A 345 (2003) 81-89.

[16] V. Gridnev, V. Nemoshkalenko, Y. Meshkov, V. Gavrilyuk, V. Prokopenko, O. Razumov,

Mössbauer effect in deformed Fe–C alloys, physica status solidi (a) 31 (1975) 201-210.

[17] V. Gridnev, V. Gavrilyuk, I.Y. Dekhtyar, Y. Meshkov, P. Nizin, V. Prokopenko, Investigation of carbide phase in strained steel by the method of nuclear gamma resonance, physica status solidi (a) 14 (1972) 689-694.

[18] J. Languillaume, G. Kapelski, B. Baudelet, Cementite dissolution in heavily cold drawn pearlitic steel wires, Acta Mater. 45 (1997) 1201-1212.

[19] X. Sauvage, J. Copreaux, F. Danoix, D. Blavette, Atomic-scale observation and modelling of cementite dissolution in heavily deformed pearlitic steels, Phil. Mag. A 80 (2000) 781-796.

[20] G.A. Nematollahi, J. von Pezold, J. Neugebauer, D. Raabe, Thermodynamics of carbon solubility in ferrite and vacancy formation in cementite in strained pearlite, Acta Mater. 61 (2013) 1773-1784.

[21] Q.H. Li, C. Zhang, H. Chen, H. Chen, Z.G. Yang, Microstructural Evolution of a Hypoeutectoid Pearlite Steel under Rolling-sliding Contact Loading, J. Iron Steel Res. Int. 23 (2016) 1054-1060.

[22] A. Kapoor, F. Franklin, Tribological layers and the wear of ductile materials, Wear 245 (2000) 204-215.

[23] F. Franklin, I. Widiyarta, A. Kapoor, Computer simulation of wear and rolling contact fatigue, Wear 251 (2001) 949-955.

[24] A. Bower, Cyclic hardening properties of hard-drawn copper and rail steel, Journal of the Mechanics and Physics of Solids 37(4) (1989) 455-470.

[25] W. Tyfour, J. Beynon, A. Kapoor, The steady state wear behaviour of pearlitic rail steel under dry rolling-sliding contact conditions, Wear 180(1-2) (1995) 79-89.

[26] K. Nakajima, M. Apel, I. Steinbach, The role of carbon diffusion in ferrite on the kinetics of cooperative growth of pearlite: a multi-phase field study, Acta Mater. 54 (2006) 3665-3672.

[27] A. Yamanaka, T. Takaki, Y. Tomita, Coupled simulation of microstructural formation and deformation behavior of ferrite–pearlite steel by phase-field method and homogenization method, Mater. Sci. Eng. A 480 (2008) 244-252.

[28] K. Ankit, A. Choudhury, C. Qin, S. Schulz, M. McDaniel, B. Nestler, Theoretical and numerical study of lamellar eutectoid growth influenced by volume diffusion, Acta Mater. 61 (2013) 4245-4253.

[29] S.G. Kim, W.T. Kim, T. Suzuki, Phase-field model for binary alloys, Phys. Rev. e 60 (1999) 7186.

[30] M. Enomoto, H. Aaronson, On the critical nucleus composition of ferrite in an Fe-C-Mn alloy, Metall. Trans. A 17(8) (1986) 1381-1384.

[31] I. Loginova, J. Odqvist, G. Amberg, J. Ågren, The phase-field approach and solute drag modeling of the transition to massive $\gamma \rightarrow \alpha$ transformation in binary Fe-C alloys, Acta Mater. 51 (2003) 1327-1339.

[32] I. Loginova, J. Ågren, G. Amberg, On the formation of Widmanstätten ferrite in binary Fe–C–phase-field approach, Acta Mater. 52 (2004) 4055-4063.

[33] T. Ohashi, L. Roslan, K. Takahashi, T. Shimokawa, M. Tanaka, K. Higashida, A multiscale approach for the deformation mechanism in pearlite microstructure: Numerical evaluation of elasto-plastic deformation in fine lamellar structures, Mater. Sci. Eng. A 588 (2013) 214-220.

[34] J.W. Cahn, J.E. Hilliard, Free energy of a nonuniform system. I. Interfacial free energy, J. Chem. Phys. 28 (1958) 258-267.

[35] S.M. Allen, J.W. Cahn, A microscopic theory for antiphase boundary motion and its application to antiphase domain coarsening, Acta Metall. 27 (1979) 1085-1095.

[36] S.Y. Hu, J. Murray, H. Weiland, Z.K. Liu, L.-Q. Chen, Thermodynamic description and growth kinetics of stoichiometric precipitates in the phase-field approach, Calphad 31 (2007) 303-312.

[37] X. Sauvage, Y. Ivanisenko, The role of carbon segregation on nanocrystallisation of pearlitic steels processed by severe plastic deformation, Journal of materials science 42 (2007) 1615-1621.

[38] C.J. Huang, D.J. Browne, S. McFadden, A phase-field simulation of austenite to ferrite transformation kinetics in low carbon steels, Acta Mater. 54 (2006) 11-21.

[39] J. Zhu, L.-Q. Chen, J. Shen, V. Tikare, Coarsening kinetics from a variable-mobility Cahn-Hilliard equation: Application of a semi-implicit Fourier spectral method, Phys. Rev. E 6 (1999) 3564.

[40] L.-Q. Chen, J. Shen, Applications of semi-implicit Fourier-spectral method to phase field equations, Comput. Phys. Commun.108 (1998) 147-158.

[41] Y. Li, P. Choi, C. Borchers, S. Westerkamp, S. Goto, D. Raabe, R. Kirchheim, Atomic-scale mechanisms of deformation-induced cementite decomposition in pearlite, Acta Mater. 59 (2011) 3965-3977.

[42] A. Hohenwarter, A. Taylor, R. Stock, R. Pippan, Effect of large shear deformations on the fracture behavior of a fully pearlitic steel, Metall. Mater. Trans. A 42 (2011) 1609-1618.

[43] X. Zhang, A. Godfrey, N. Hansen, X. Huang, Hierarchical structures in cold-drawn pearlitic steel wire, Acta Mater. 61 (2013) 4898-4909.

[44] M. Hong, W. Reynolds, T. Tarui, K. Hono, Atom probe and transmission electron microscopy investigations of heavily drawn pearlitic steel wire, Metall. Mater.Trans. A 30 (1999) 717-727.

[45] G. Baumann, H. Fecht, S. Liebelt, Formation of white-etching layers on rail treads, Wear 191 (1996) 133-140.

Figure Captions

Fig. 1. (a) Schematic description of plastic deformation induced free energy increase; and (b) molar free energies of ferrite and cementite as a function of carbon content; c^{α} and c_{ε}^{α} refer to the equilibrium carbon content in ferrite before and after deformation, respectively; and schematic description of cementite dissolution in inserted picture.

Fig. 2. Cementite dissolution behavior simulated by present phase-field model with ferrite/cementite interface thickness of 4 nm, by Sauvage's model [19] and of experiment results [12] in cold-drawn wires; and cementite dissolution behavior with different ferrite/cementite interface thicknesses (2 nm, 1.8 nm, 1.6 nm, 1.4 nm and 1.3 nm). Carbon concentration across ferrite/cementite interface based on sharp interface assumption [19], present diffusion interface assumption and experiment measurement [41] in inserted picture.

Fig. 3. (a) Shear stress distribution of sample under rolling-sliding loading; (b) magnified view of the vicinity of contact region; (c) maximum shear stress distribution with depth (The maximum shear stress at a specific depth is obtained by searching the maximum value of shear stress at this depth.); and (d) accumulated plastic shear strain as a function of rolling cycles at the contact depth of 0 μm,10 μm, 20 μm, 30 μm, 40 μm, 60 μm, and 100 μm.

Fig. 4. Simulated microstructure morphology of pearlite after different rolling cycles and at different contact depths; and dot circles indicate the initiation of discontinuity or breakage in the cementite lamellae.

Fig. 5. TEM micrographs of sample after 120000 rolling cycles (a) at the center of sample; (b) at the depth of 10 μm; (d) at the depth of 20 μm and (e) the corresponding HRTEM. (c) and (f) simulated microstructure for depth of 10 μm and 20 μm, respectively.

Fig. 6. Simulated cementite lamellae thickness evolved with (a) rolling cycles and with (b) contact depths; and SEM micrographs of longitudinal sections of samples after (c) 30000 rolling cycles, and (d) 120000 rolling cycles.

Fig. 7. Simulated carbon concentration profiles across cementite lamellae as a function of rolling cycles at depth of (a) 0 μm; (b) 10 μm; (c) 20 μm; and (d) simulated carbon concentration profile at depth of 10 μm after 51150 cycles comparing with experimental measured carbon concentration on rail surface [6].

Fig. 8. (1) Simulated cementite dissolution kinetics and the corresponding carbon distribution in a–h; and (2) simulated cementite dissolution behavior across the transition zone, i.e. at the depth of 10 μm, 12.5 μm, 15 μm, 17.5 μm and 20 μm.

Fig. 9. Simulated cementite volume fraction as a function of rolling cycles with and without the elastic strain-induced free energy increase at the depth of 0 μm, 10 μm and 20 μm.

Fig. 10. Simulated carbon volume fraction for different interface thicknesses (2 nm, 3 nm, 4 nm, 5 nm and 6 nm) at different contact depths (0 μm, 10 μm, and 20 μm) as a function of rolling cycles, same color refers to the same interface thickness. (For interpretation of the references to color in this figure legend, the reader is referred to the web version of this article.)

Fig. 11. Simulated cementite volume fraction as a function of rolling cycles for different initial cementite lamellar thicknesses.

Table Captions

Table 1 Experiment parameters of rolling-sliding contact conditions

Table 2 Model parameters and related quantities

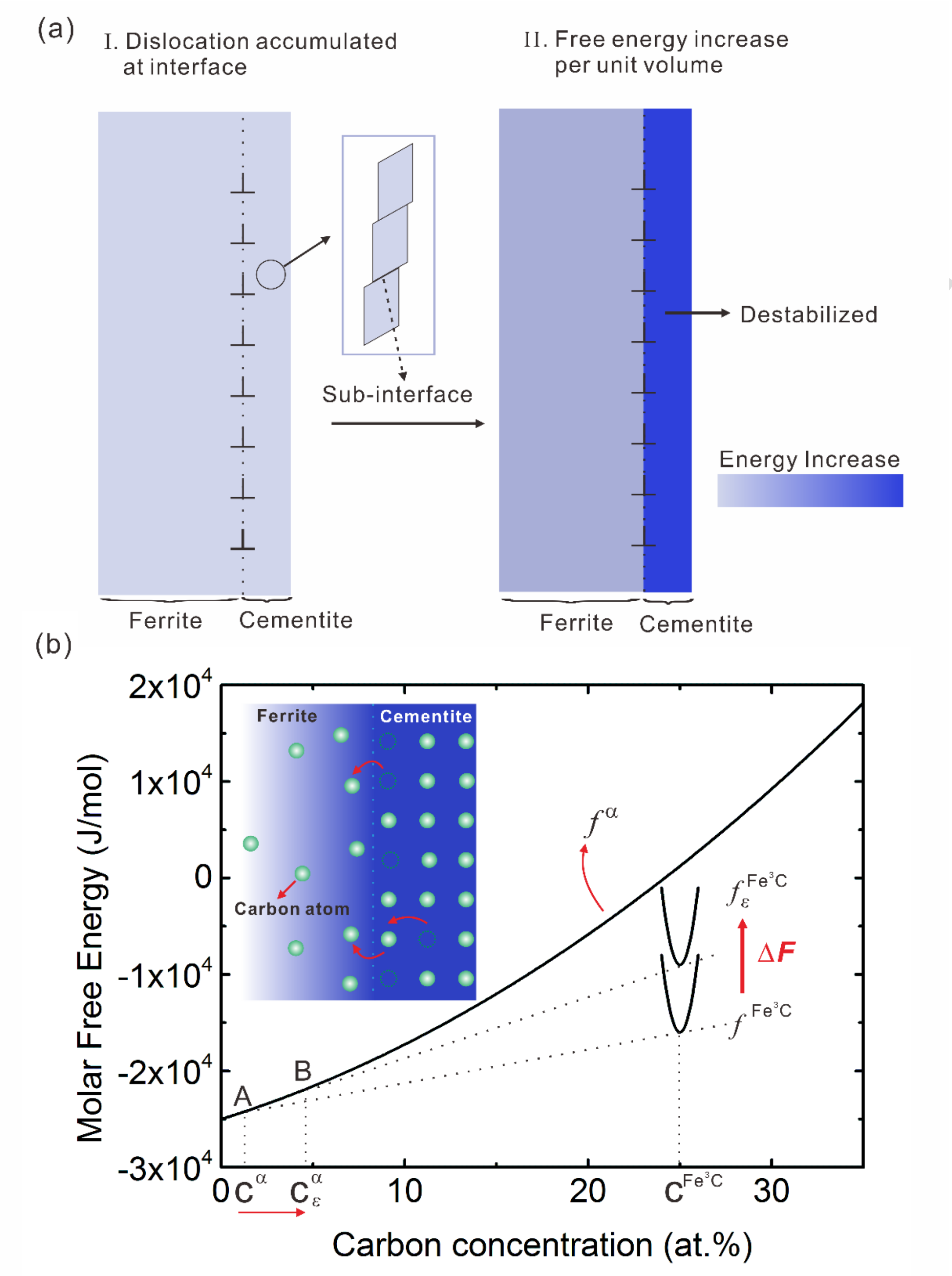

Fig. 1. (a) Schematic description of plastic deformation induced free energy increase; and (b) molar free energies of ferrite and cementite as a function of carbon content; c^{α} and c_{ε}^{α} refer to the equilibrium carbon content in ferrite before and after deformation, respectively; and schematic description of cementite dissolution in inserted picture.

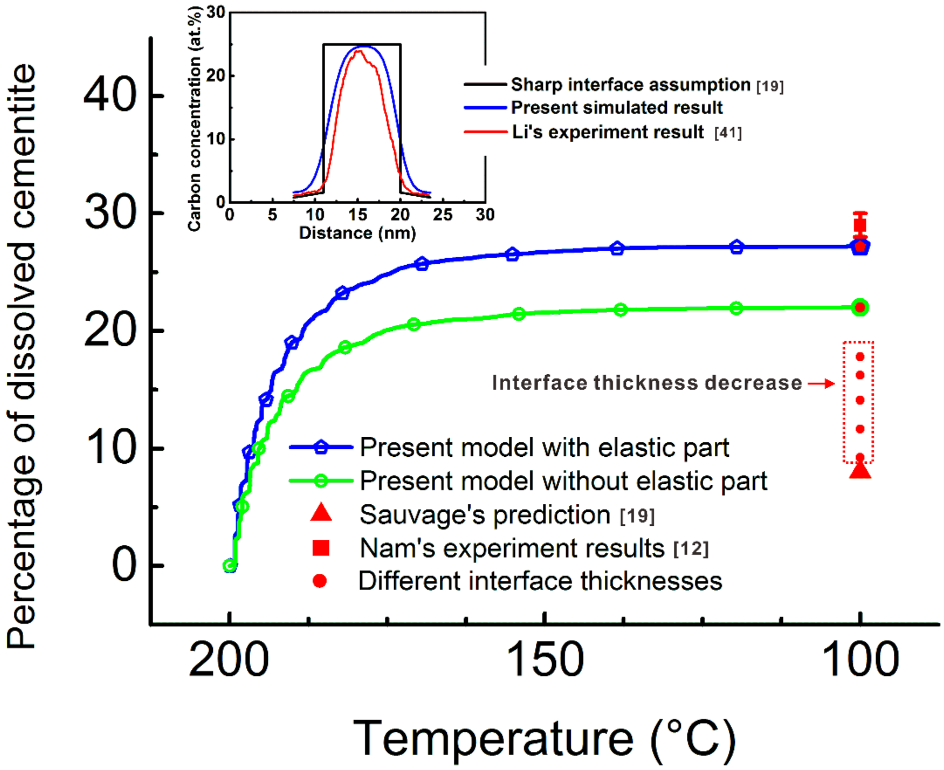

Fig. 2. Cementite dissolution behavior simulated by present phase-field model with ferrite/cementite interface thickness of 4 nm, by Sauvage's model [19] and of experiment results [12] in cold-drawn wires; and cementite dissolution behavior with different ferrite/cementite interface thicknesses (2 nm, 1.8 nm, 1.6 nm, 1.4 nm and 1.3 nm). Carbon concentration across ferrite/cementite interface based on sharp interface assumption [19], present diffusion interface assumption and experiment measurement [41] in inserted picture.

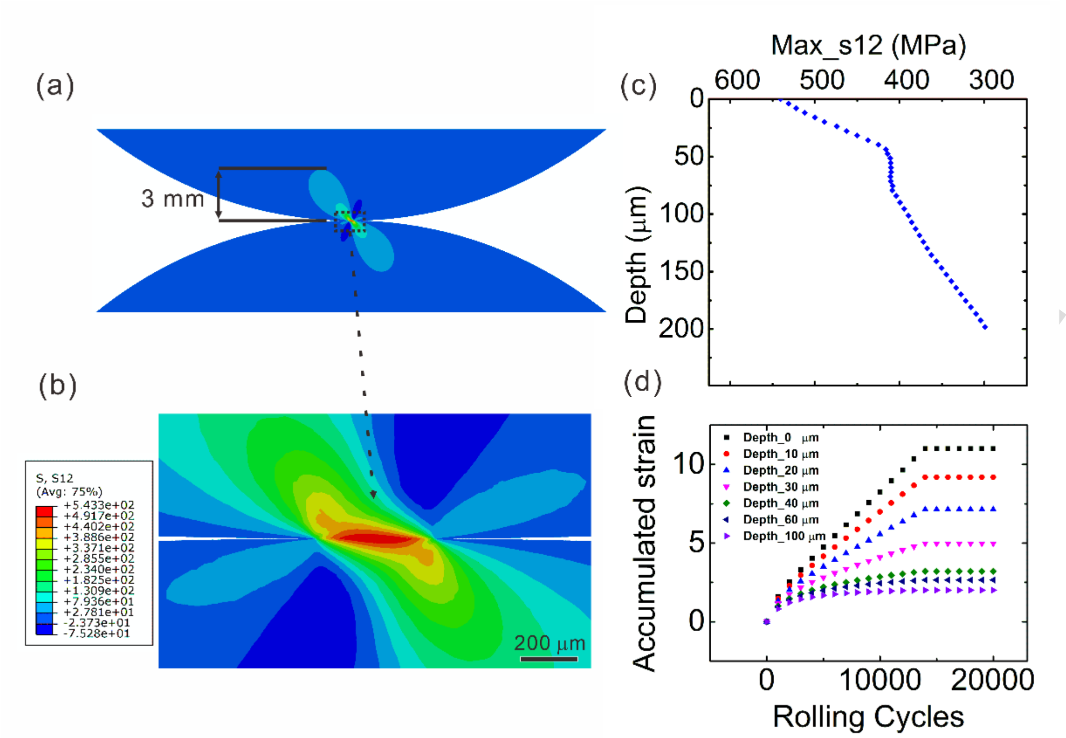

Fig. 3. (a) Shear stress distribution of sample under rolling-sliding loading; (b) magnified view of the vicinity of contact region; (c) maximum shear stress distribution with depth (The maximum shear stress at a specific depth is obtained by searching the maximum value of shear stress at this depth.); and (d) accumulated plastic shear strain as a function of rolling cycles at the contact depth of 0 μm,10 μm, 20 μm, 30 μm, 40 μm, 60 μm, and 100 μm.

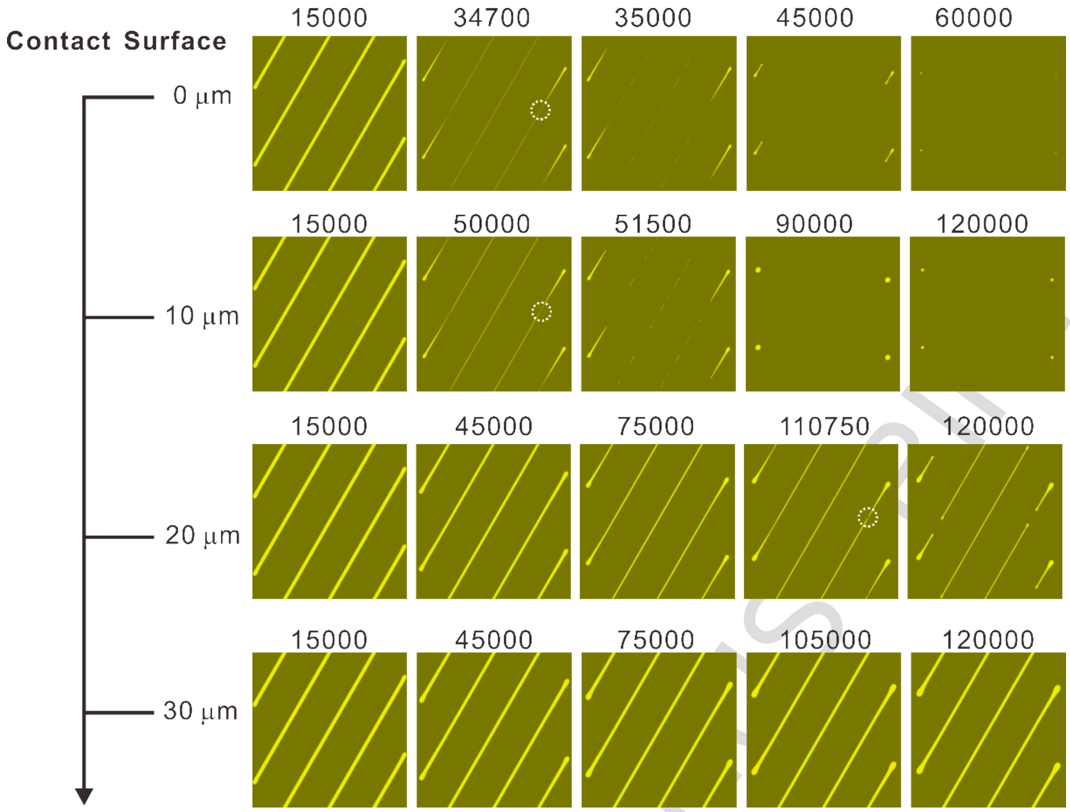

Fig. 4. Simulated microstructure morphology of pearlite after different rolling cycles and at different contact depths; and dot circles indicate the initiation of discontinuity or breakage in the cementite lamellae.

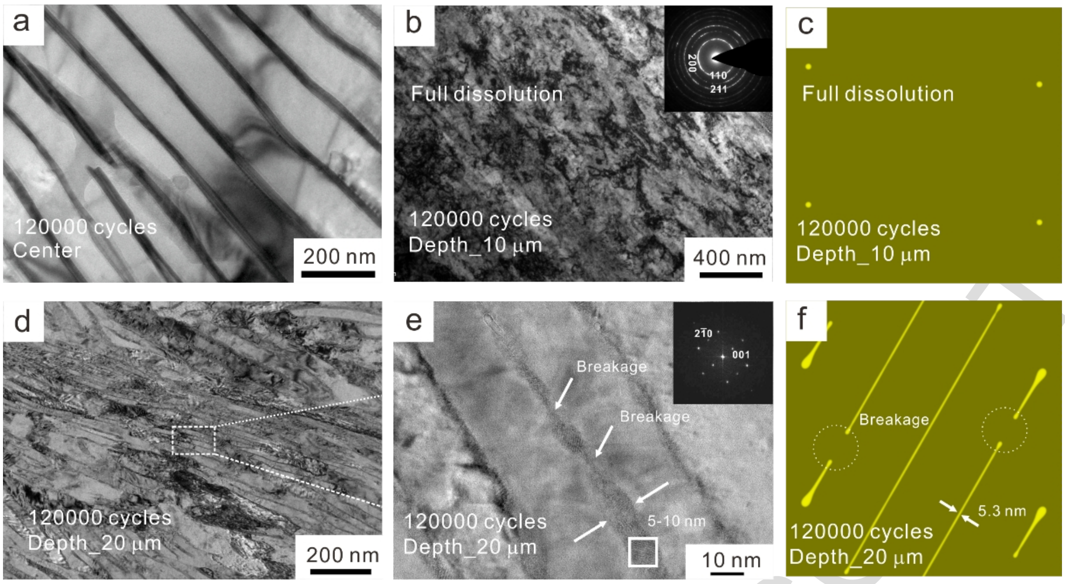

Fig. 5. TEM micrographs of sample after 120000 rolling cycles (a) at the center of sample; (b) at the depth of 10 μm; (d) at the depth of 20 μm and (e) the corresponding HRTEM. (c) and (f) simulated microstructure for depth of 10 μm and 20 μm, respectively.

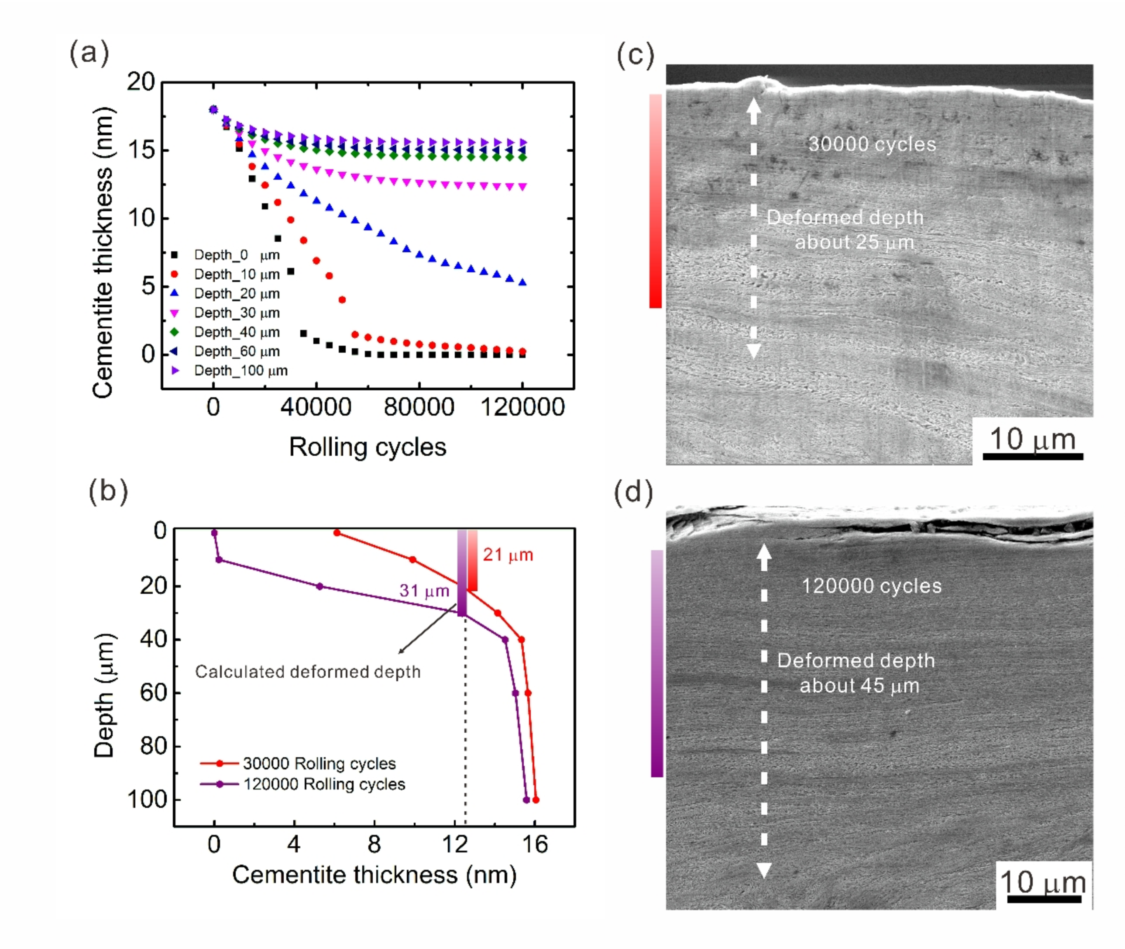

Fig. 6. Simulated cementite lamellae thickness evolved with (a) rolling cycles and with (b) contact depths; and SEM micrographs of longitudinal sections of samples after (c) 30000 rolling cycles, and (d) 120000 rolling cycles.

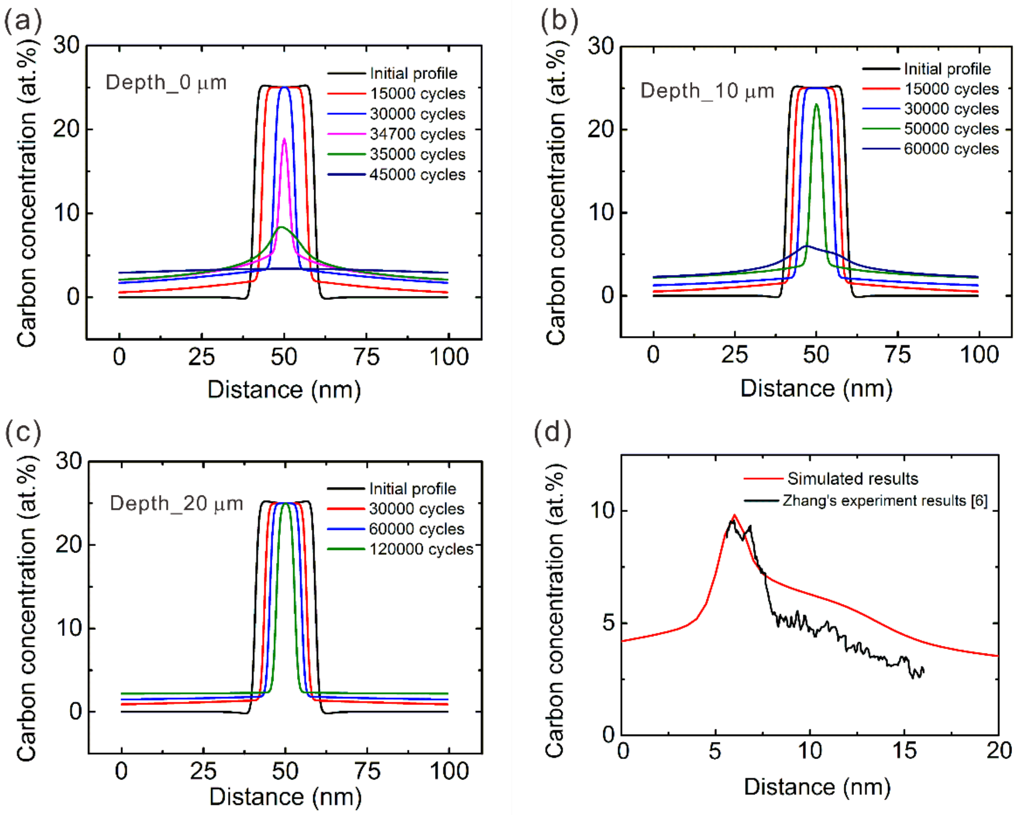

Fig. 7. Simulated carbon concentration profiles across cementite lamellae as a function of rolling cycles at depth of (a) 0 μm; (b) 10 μm; (c) 20 μm; and (d) simulated carbon concentration profile at depth of 10 μm after 51150 cycles comparing with experimental measured carbon concentration on rail surface [6].

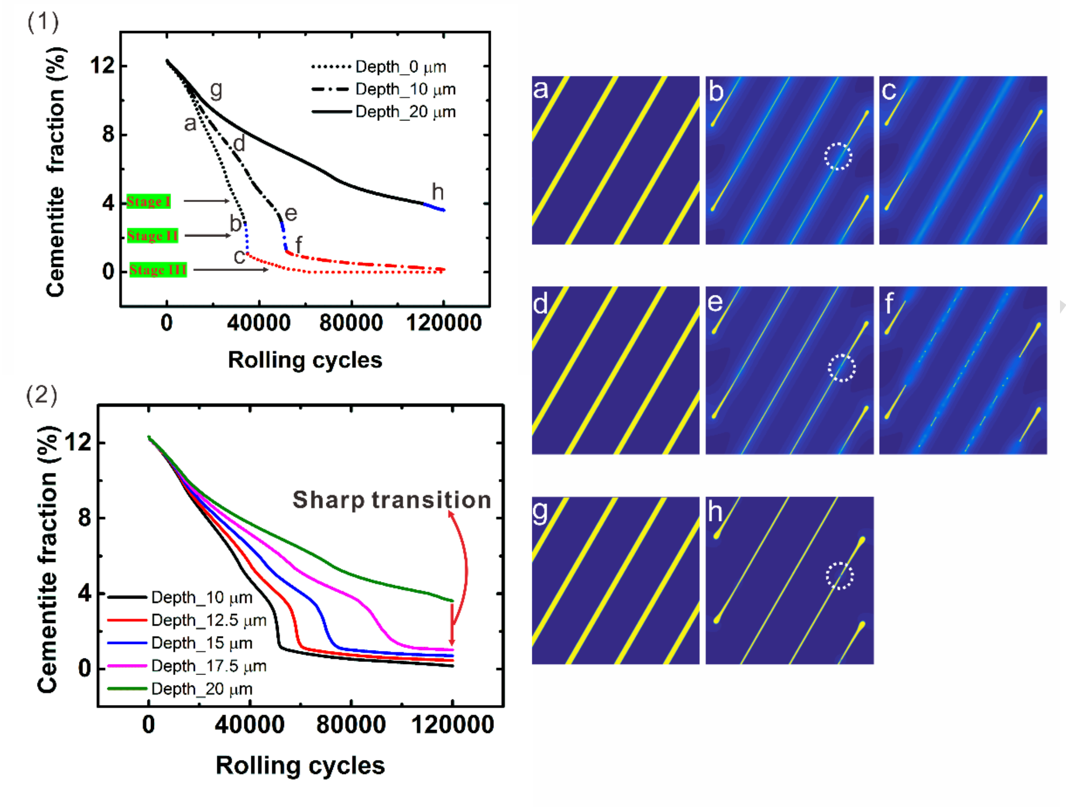

Fig. 8. (1) Simulated cementite dissolution kinetics and the corresponding carbon distribution in a–h; and (2) simulated cementite dissolution behavior across the transition zone, i.e. at the depth of 10 μm, 12.5 μm, 15 μm, 17.5 μm and 20 μm.

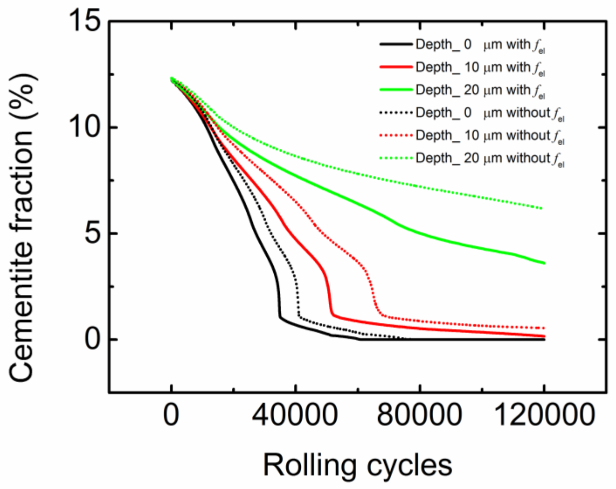

Fig. 9. Simulated cementite volume fraction as a function of rolling cycles with and without the elastic strain-induced free energy increase at the depth of 0 μm, 10 μm and 20 μm.

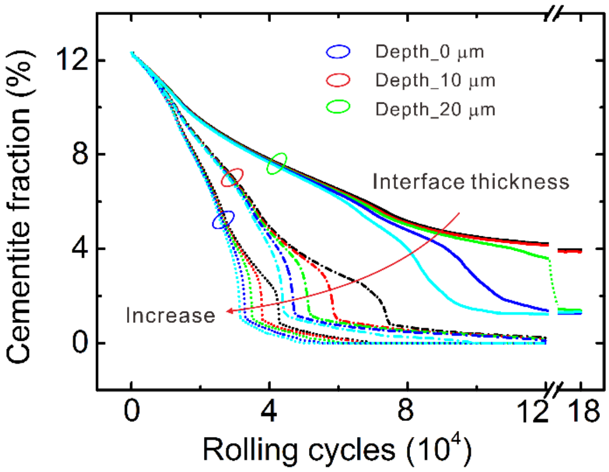

Fig. 10. Simulated carbon volume fraction for different interface thicknesses (2 nm, 3 nm, 4 nm, 5 nm and 6 nm) at different contact depths (0 μm, 10 μm, and 20 μm) as a function of rolling cycles, same color refers to the same interface thickness. (For interpretation of the references to color in this figure legend, the reader is referred to the web version of this article.)

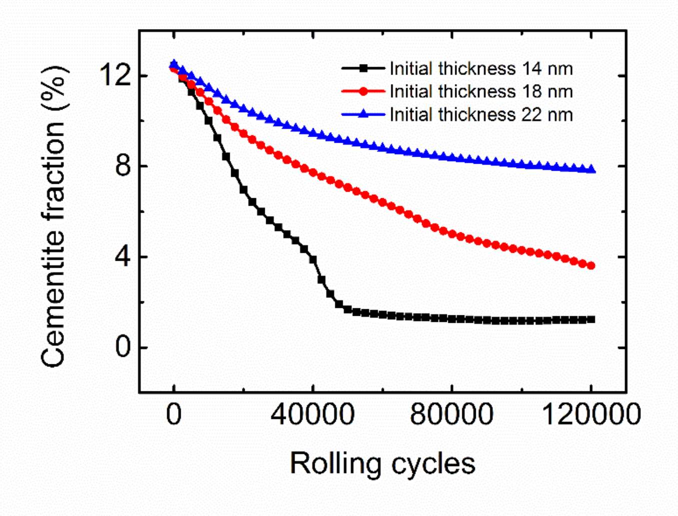

Fig. 11. Simulated cementite volume fraction as a function of rolling cycles for different initial cementite lamellar thicknesses.

Table 1 Experiment parameters of rolling-sliding contact conditions.

Sample	Load (N)	Up disc speed (rpm)	Bottom disc speed (rpm)	Sliding Ratio (%)	Rolling cycles
A	1500	500	497.5	0.5	30000
B	1500	500	497.5	0.5	120000

Table 2 Model parameters and related quantities.

Model parameters	**Symbol**	**Value**	**Ref.**
Fitting parameters for ferrite	A^{α}	7.25×10^{5} J/mol	[20]
	B^{α}	-3198.3 J/mol	[20]
	C^{α}	19.8 J/mol	[20]
Fitting parameters for cementite	$A^{\mathrm{Fe_3C}}$	2.73×10^{6} J/mol	[20]
	$B^{\mathrm{Fe_3C}}$	-5049.9 J/mol	[20]
	$C^{\mathrm{Fe_3C}}$	-3.7 J/mol	[20]
Molar volume of the system	Ω_0	6.91×10^{-6} m^{3}mol^{-1}	[30]
Molar volume of cementite	V_m	5.84×10^{-6} m^{3}mol^{-1}	[19]
Physical interface mobility	M_p	9.0×10^{-16} m^4/Js	[26]
Interfacial energy	γ	1.0 J/m^2	[26]
Prefactor of carbon diffusion constant in ferrite	D_0	2.2×10^{-4} m^2/s	[26]
Activation energy of carbon diffusion in ferrite	Q	122.5 kJ/mol	[26]
Interface thickness	2λ	4 nm	
Simulation time step	t^*	1.05×10^{-5} s	
Contact time in one cycle	t_c	1.91×10^{-4} s	